

**Image-potential states of single- and multiwalled carbon nanotubes**

M. Zamkov, H. S. Chakraborty, A. Habib, N. Woody, U. Thumm, and P. Richard

*James R. Macdonald Laboratory, Department of Physics, Kansas State University, Manhattan, Kansas 66506-2604, USA*

(Received 8 October 2003; revised manuscript received 12 April 2004; published 28 September 2004)

The existence of low angular momentum image-potential states is predicted both for single- and multiwalled nanotubes. The states are confined between the self-induced potential on the vacuum side and the surface barrier, created by the central ascent in the transverse nanotube potential. Effective interactions near the surface of the nanotube are modeled with a cylindrical jelliumlike surface barrier, parameterized to ensure the correct transition into the long-range image potential. Binding energies and wave functions are calculated for (12,0), (10,10), (9,0) single-walled and ( $d=9.48$  nm) multiwalled nanotubes for different values of electron angular momenta. In addition, the expected relative lifetimes were calculated for the case of zero-angular momentum states of a (10,10) SWNT. The possible formation of image-potential states in nanotube bundles is briefly discussed.

DOI: 10.1103/PhysRevB.70.115419

PACS number(s): 73.21.Hb

**I. INTRODUCTION**

The studies of image-potential states at surfaces and interfaces provided a tool for probing the electronic structure and dynamics on a nanometer scale.<sup>1–4</sup> These states are formed when an excess electron induces an image charge and becomes trapped in the attractive potential of the locally polarized surface. For some years, the investigation of image states was mainly performed on clean metal surfaces and surfaces with overlayers. Recently, advances in the fabrication of nanostructured materials enabled an exploration of these states in a variety of nanoscopic settings including molecular nanowires<sup>5,6</sup> and liquid He.<sup>7,8</sup>

In the work of Granger *et al.*,<sup>9</sup> a class of image-potential states has been predicted to exist around the surfaces of freely suspended linear molecular conductors or dielectrics, such as carbon nanotubes. In contrast to the confinement nature of image states above metal surfaces, where the electron's motion is localized between the attractive image potential and a band gap along the surface normal, the *tubular* image states in Ref. 9, are produced with a nonzero-angular momentum ( $l \geq 6$ ), so that the resulting positive centrifugal barrier keeps the electronic wave functions away from the tube. Binding energies and wave functions of these image states were calculated for the case of a (10,10) single-walled nanotube (SWNT). It was concluded that due to a weak interaction of “over-the-barrier” states with the surface of a nanotube, their lifetimes are expected to be much longer than those of surface image-potential states in metals.

The experimental observation of tubular image states, however, poses tremendous challenges. Since these states are formed at distances of at least 10 nm from the nanotube, the latter needs to be isolated from any source of interaction, such as a substrate or other SWNTs. Synthesis of the adequate size sample with described characteristics is not an easy task<sup>10</sup> and is complicated even more by the tendency of SWNTs to form bundles (ropes). The excitation of tubular image states in suspended SWNT networks<sup>11</sup> seems to be the future prospective. At the present time, however, the amount of nanotubes in these samples is still insufficient for the observation of the described feature.

In this paper, it is demonstrated that both SWNTs and multiwalled nanotubes (MWNTs) can support image-potential states directly in front of the surface. These states are confined between the self-induced potential on the vacuum side and the potential barrier inside the nanotube. Binding energies of the investigated states are located significantly lower below the vacuum level than those of tubular image states, resulting in substantially smaller radii of localization. This makes them far less susceptible to external perturbations caused, for example, by interactions with the substrate or impurities.

We model effective short-range interactions between the surface of the nanotube and an image electron by introducing a cylindrical jelliumlike potential barrier, parameterized to ensure the correct behavior at the bulk–vacuum interface. Previously, the jellium barrier model has been employed for characterization of one or several monolayer systems, such as fullerenes<sup>12,13</sup> and thin films.<sup>14</sup> Its success in predicting the correct positions of weakly bound electronic states, promotes the use of the cylindrical jellium for modeling the electron–surface interactions in nanotubes.

Binding energies and wave functions were calculated for (12,0), (10,10), (9,0) SWNTs and a ( $d=9.48$  nm) MWNT for an electron angular momentum in the range of  $l=0–10$ . Present results indicate that variations in the nanotube diameter have a unique effect on energies of the calculated image-potential states, which is primarily attributed to the difference in the long-range behavior of the induced and centrifugal parts of the total effective potential for the system. Values of the minimal angular momentum required for the formation of the repulsive centrifugal barrier are compared for different SWNTs and MWNTs. Analysis using the wave function's penetration into the bulk is found to provide an approximate estimate of the lifetime. In addition, the possible formation of image-potential states in nanotube bundles is investigated.

**II. THEORETICAL MODEL**

In this section, we describe a one-electron potential for a nanotube of radius  $a$ . Owing to the cylindrical symmetry of a

SWNT, the electron's motion in the  $z$  direction can be separated:

$$\Psi_{n,l,k}(\rho, \phi, z) = \frac{1}{\sqrt{2\pi\rho}} \psi_{n,l}(\rho) e^{il\phi} e^{ikz}, \quad (1)$$

where  $l$  is the angular momentum of an electron with respect to the axis of a nanotube. The resulting one-dimensional problem is solved to obtain the binding energies,  $E_{n,l}$ , and the wave functions  $\psi_{n,l}(\rho)$  for the electron motion in the transverse direction. In Eq. (1), the electron is assumed to move freely along the nanotube, such that the energy  $E_k$  associated with the motion in the  $z$  direction is a continuous variable. The possible presence of impurities or defects that may result in electron's localization causing the quantization of  $E_k$  (Ref. 9) is not taken into account.

Directly in front of the surface of a nanotube the form of the potential will be dominated by the repulsive surface barrier that keeps an electron from decaying into bulk. This short-range interaction vanishes at large distances, where the electron primarily experiences the long-range image potential, modified by the presence of the centrifugal force.

The form of the three-dimensional image potential,  $V_{\text{Im}}$ , induced by an electron approaching a nanotube, is given by Ref. 15:

$$V_{\text{Im}}(\rho', \phi, z) = -\frac{2e}{\pi} \sum_{m=-\infty}^{m=+\infty} \int_0^{\infty} dk \cos(kz) \exp(\text{Im } \phi) \times \frac{I_m(ka)}{K_m(ka)} K_m(k\rho) K_m(k\rho'), \quad (2)$$

where the electron is located outside the tube of radius  $a$  at the position  $(\rho, 0, 0)$ , and  $I_m(x)$  and  $K_m(x)$  are the regular and irregular Bessel functions. The long-range character as well as the correct limiting behavior of this potential can be reproduced with the sufficient accuracy by introducing the following approximate form:<sup>9</sup>

$$V_{\text{Im}}(\rho) \approx \frac{2e^2}{\pi a} \sum_{n=1,3,5,\dots} li[(a/\rho)^n], \quad (3)$$

where  $li(x) \equiv \int_0^x dt/\ln(t)$ . Note that  $V_{\text{Im}}(\rho)$  is singular at  $\rho = a$ .

The total long-range potential,  $V_{\text{LR}}$ , is then obtained by combining the image potential of Eq. (3) and the centrifugal interaction in the following manner:

$$V_{\text{LR}}(\rho) \approx \frac{2e^2}{\pi a} \sum_{n=1,3,5,\dots} li[(a/\rho)^n] + \frac{(l^2 - \frac{1}{4})}{2m_e \rho^2}, \quad (4)$$

where  $l$  is the angular momentum of the state and  $m_e$  is the reduced mass of an electron.

In order to describe the short-range potential near the surface of the tube, we adopt the jellium barrier model for the metallic film in the analytic form of Jennings *et al.*,<sup>14</sup> modified to describe the interfaces on both sides of the film:<sup>16</sup>

$$V(z) = \begin{cases} \frac{-1}{4(|z| - z_0)} [1 - e^{-\lambda(|z| - z_0)}] & |z| > z_0 \\ \frac{-U_0}{Ae^{\beta(|z| - z_0)} + 1}, & |z| \leq z_0, \end{cases} \quad (5)$$

where  $z=0$  corresponds to the midpoint of the film and  $z=z_0$  is identified with the location of the image plane for static charges.<sup>17</sup> The constants  $A$  and  $\beta$  are determined by matching  $V(z)$  and its derivative at  $z=z_0$ , and the adjustable parameter  $U_0$  defines the depth of the jellium potential well. The remaining quantity,  $\lambda$ , determines the transition range ( $1/\lambda$ ) over which the barrier saturates. This simple barrier model was shown to reproduce well the effective electron potential at different surfaces obtained from density functional calculations.<sup>14,18</sup>

For a SWNT, the *full* effective surface potential is constructed in a similar way on both sides of the infinitely long cylindrical shell of thickness  $\Delta R$ :

$$V_{\text{eff}}(\rho) = \begin{cases} V_{\text{LR}}(\rho^+) [1 - e^{-\lambda|\rho - \rho_0^-|^n}] & \rho < \rho_0^- \\ \frac{-U_0}{A_l e^{-\beta_l|\rho - \rho_0^\pm|} + 1} & |\rho - a| \leq \Delta R/2 \\ V_{\text{LR}}(\rho^-) [1 - e^{-\lambda|\rho - \rho_0^+|^n}] & \rho > \rho_0^+, \end{cases} \quad (6)$$

where  $\rho^\pm = \rho \pm \Delta R/2$ , and  $\rho_0^\pm = a \pm \Delta R/2$  define the location of the image reference plane on either side of the tube's wall. Since  $A_l$  and  $\beta_l$  are determined via the matching at these planes, they depend on the angular momentum  $l$ . We adopt the same shell thickness,  $\Delta R$ , of 0.296 nm as in the case of a spherical carbon cage used for constructing the  $C_{60}$  jellium.<sup>13</sup>

The parameter  $U_0$ , defining the depth of the potential well was obtained by requiring that bound state energies of the model system are appropriate for the highest occupied states in carbon nanotubes, located well below the energies of image state electrons. The density of states for the valence bands has been well established both theoretically and experimentally<sup>19-22</sup> and is used here as a reference of nanotube electronic properties. Since each level of the one-dimensional jellium well can be populated by two electrons, the four valence electrons of the carbon atom,  $2s^2$  and  $2p^2$  will fully occupy the available  $n=1$  and  $n=2$  levels. In this case, the jellium Fermi level should be located close to the energy of  $n=2$  state,  $E_F \approx E_{n=2}$ . The value of  $U_0$ , therefore, is adjusted to match the  $n=2$  level with the Fermi energy of a carbon nanotube. For  $U_0 = -15.24$  eV, the energies of  $n=1$  and  $n=2$  levels become  $-12.41$  eV and  $-5.7$  eV, respectively, where the latter is consistent with the Fermi energy, averaged over different geometries of metallic carbon nanotubes. In principle, small variations of the Fermi level within different nanotube chiralities<sup>21</sup> can be accounted for in the jellium potential by varying  $U_0$ . However, since positions of the image-potential states relative to the vacuum level are essentially unaffected by slight changes in  $E_F$ ,<sup>23</sup> the same jellium depth is used for all carbon nanotubes investigated in this work.

The singularities in  $V_{\text{Im}}$  [Eq. (3)] at  $\rho = a \pm \Delta R/2$  are avoided in a manner similar to that of a  $1/z$  potential in

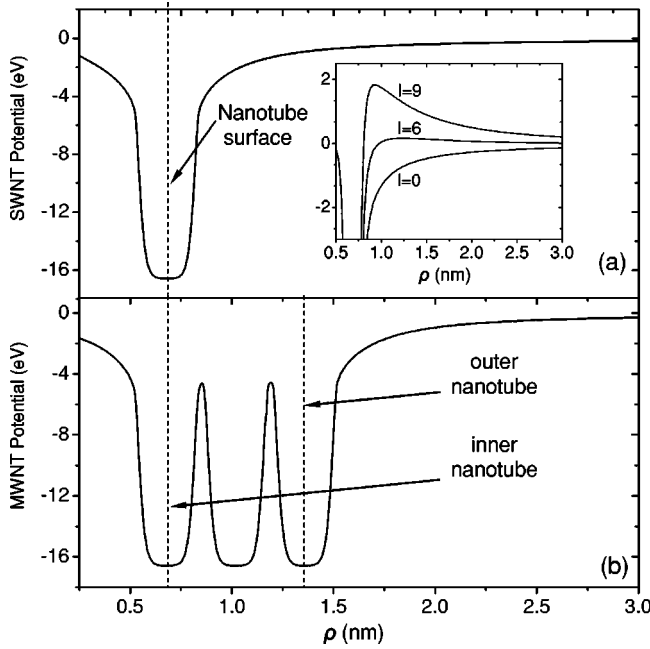


FIG. 1. The total effective potential for an  $l=1$  image electron in the vicinity of a SWNT (a) and MWNT (b). The inset in (a) displays the effective potential for different values of electron angular momenta.

metallic films. We assume that the divergence in  $V_{\text{im}}$  can be represented as some power  $\nu$  of  $1/[\rho - \rho_0]$ , ( $\nu > 0$ ). Hence, the limiting value of  $V_{\text{eff}}(\rho)$  for  $\rho \rightarrow \rho_0^+ + 0$  is given by the L'Hospital's rule:

$$\lim_{\rho \rightarrow \rho_0^{\pm 0}} \frac{1 - e^{-\lambda|\rho - \rho_0|^\nu}}{|\rho - \rho_0|^\nu} = \lambda. \quad (7)$$

The parameter  $\nu$ , which, in the case of the film potential equals 1, was determined numerically by requiring that the saturated potential,  $V_{\text{LR}}(\rho)[1 - e^{-\lambda|\rho - \rho_0|^\nu}]$ , is continuous in the vicinity of  $\rho_0$ . In the present work, the value of  $\nu$  was found to be 0.94.

Note that the image potential inside the nanotube [top panel in Eq. (6)] is obtained through a variable transformation,  $\rho \rightarrow 2a - \rho$ , in the potential on the vacuum side (bottom panel). According to self-consistent calculations of the radial potential for the  $C_{60}$  molecule,<sup>13</sup> the long-range “wings” are symmetric with respect to the fullerene shell. This encourages the use of the same functional form on both sides of the nanotube wall. However, since the penetration of an image state electron beyond the jellium barrier ( $\rho_0^- \leq \rho \leq \rho_0^+$ ) is expected to be weak, the small differences of the inner potential from the outer should have very little effect on binding energies of image states.

The effective potential  $V_{\text{eff}}(\rho)$ , calculated for an  $l=1$  image electron in the presence of a (10,10) SWNT ( $a = 0.68$  nm) is shown in Fig. 1(a). The associated matching parameters in this case are  $A_1 = 1.6$  and  $\beta_1 = 3.1$ . The quantity  $\lambda$ , which defines the value of the saturated potential at the bulk-vacuum interface ( $\rho \rightarrow \rho_0 + 0$ ) is obtained by requiring that  $V_{\text{eff}}(\rho)$  is continuous near  $\rho = \rho_0$ . We note that matching

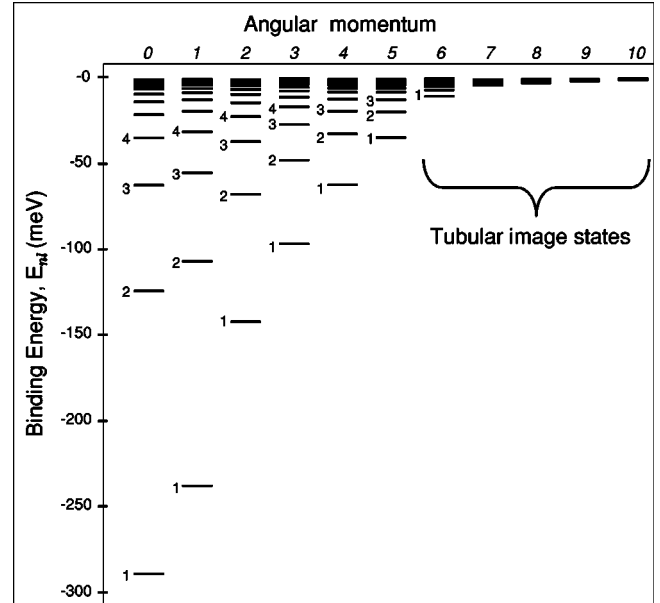


FIG. 2. Binding energies of image-potential states calculated for the (10,10) SWNT ( $a = 0.68$  nm). Series of states with angular momentum in the range of 0–10 are considered. Numbers next to the energy bars indicate principal quantum numbers,  $n$ .

of the two parts in  $V_{\text{eff}}$  [see Eq. (6)] relates  $\lambda$  to both  $U_0$  and  $A_l$ . For the potential shown in Fig. 1,  $\lambda$  is found to be  $0.44a_0^{-1}$ , where  $a_0$  is the atomic unit of the length. The inset in Fig. 1 displays the dependence of a centrifugal barrier on the electron's angular momentum  $l$ .

For a MWNT, considered as a collection of concentric SWNTs with different diameters, the potential on the vacuum side will have the same analytic form as for a SWNT [see Eq. (6)]. Clearly, in this case, the nanotube radius  $a$  should be associated with the radius of a SWNT located in the outer shell. The effective potential inside a MWNT is constructed as a superposition of individual contributions from inner nanotubes. In principle, for this arrangement, formation of energy bands in the direction perpendicular to the nanotube axis becomes possible. For an average size MWNT, however, the typical number of coaxial SWNTs is 5 to 20 and the effect of perpendicular bands can be neglected. Figure 1(b) shows the total effective potential for a three-walled carbon nanotube with the outer diameter of 2.72 nm and the intertube separation of 0.34 nm.

### III. RESULTS AND DISCUSSION

#### A. Single-walled nanotubes

Binding energies of an electron in the presence of a nanotube, calculated for the case of the (10,10) SWNT are shown in Fig. 2. Image-potential states with angular momenta in the range from 0 to 10 are considered.

Classification of the states is similar to the scheme adopted for the image states above metal surfaces, such that the lowest state localized outside of bulk is labeled as  $n=1$ . Since the effective potential inside the nanotube ( $\rho_0^- \leq \rho \leq \rho_0^+$ ) also supports a number of low-lying valence states

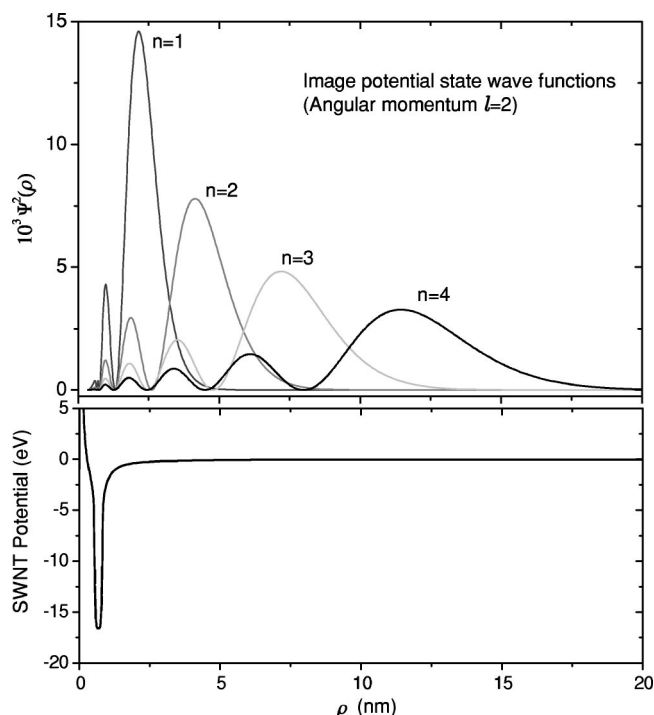


FIG. 3. Squares of the wave functions for the first four image-potential states of a (10, 10) SWNT ( $l=2$ ). The lower panel displays the associated potential in the radial direction.

with wave functions confined inside the well, image-potential state wave functions will have a number of nodes extending inside, beyond the nanotube surface (i.e.,  $\rho < a + \Delta R/2$ ). This penetration, however, is weak (see discussion at the end of the section), and the dominant part of the image electron wave function is concentrated outside of the potential well, as shown in Fig. 3. As a result, over the region outside the image reference plane ( $\rho > a + \Delta R/2$ ) the  $n=1$  state has only one transverse node. Its surface penetration is represented with a few low-amplitude nodes that are kept from extending to the nanotube center by a potential barrier at  $\rho = a - \Delta R/2$  (also see Fig. 5).

High angular momentum ( $l \geq 6$ ) states that localize behind the centrifugal barrier are marked as tubular image states in Fig. 2. Their binding energies are essentially insensitive to the potential at the nanotube surface and fully agree with the ones calculated in Ref. 9. It should be emphasized that even the group of most deeply bound tubular image states ( $n=1$ ) is located within only 12 meV away from the vacuum level, which is determined by a relatively low rise of the positive trapping potential [see the inset in Fig. 1(a)].

In contrast to tubular image states, that are isolated from the surface of the nanotube, states with small values of angular momentum experience the negative effective potential for any value of  $\rho$ , and, as a result, localize closer to the nanotube's surface, as can be seen in Fig. 3. Their binding energies are significantly deeper than those of high angular momentum states (see Fig. 2) due to much further penetration of the corresponding wave functions into the nanotube.

In comparison with image states above metal surfaces having typical binding energies in the range of 0.0–0.5 eV,<sup>3</sup>

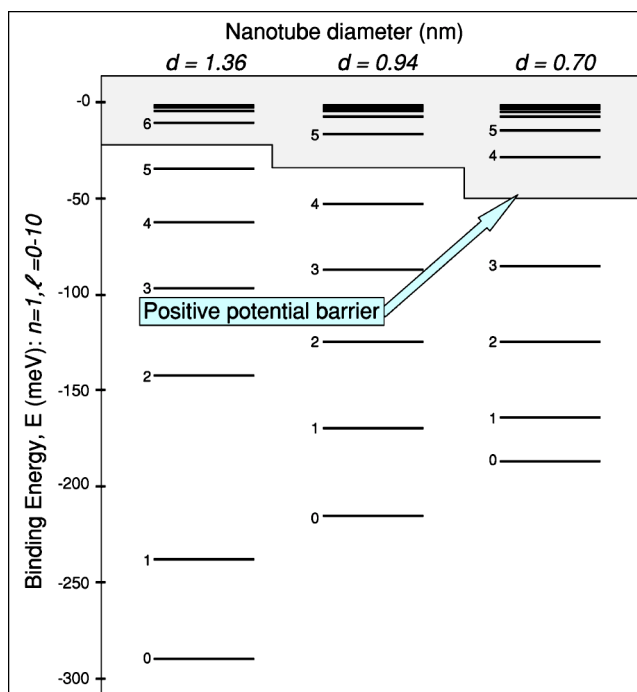


FIG. 4. Binding energies of  $n=1, l=0-10$  image-potential states calculated for the (10,10), (12,0), and (9,0) SWNTs with associated diameters of 1.36, 0.94, and 0.70 nm, respectively. The shaded area represents the location of the positive centrifugal barrier.

image states of a SWNT are located closer to the vacuum level. This difference is determined by the fact that image states above metal surfaces have a relatively large overlap with bulk states, such that their wave functions extend inside the bulk for up to 3 nm.<sup>24</sup> In the case of a SWNT, the presence of the inner wall in the nanotube jellium potential obstructs penetrations of an image electron beyond the surface to less than 1 nm.

The diameter distribution of SWNTs produced by arc discharge or laser ablation techniques is still poorly controlled. Although the latter method yields more uniform nanotubes, the typical diameter range can still be 1.0–2.0 nm.<sup>25</sup> The presence of SWNTs with different diameters in a sample results in a superposition of spectral features, such as Van Hove singularities.<sup>26</sup> In view of that, the knowledge of diameter dependent changes in a nanotube spectrum could become critical in the interpretation of experimental results. Moreover, it can be expected that binding energies will vary significantly with changes in the nanotube diameter since the effective long-range potential consists of the diameter independent centrifugal, and the diameter dependent ( $1/[(\rho/a)\ln(\rho/a)]$ ) image potential parts.

In Fig. 4, binding energies for three different types of SWNTs (10,10), (12,0), and (9,0) with associated diameters of 1.36, 0.94, and 0.70 nm, respectively, are compared. Energies of  $n=1$  image-potential states for each value of the electron angular momentum  $l$  ( $l=0-10$ ) are displayed. The shaded area represents the location of tubular image states separated from the nanotube surface by a positive centrifugal barrier. In the case of (10,10) SWNT ( $a=0.68$  nm) the minimal angular momentum needed for the presence of this bar-

rier,  $l_{\text{barrier}}$ , equals 6, as in Ref. 9. As the nanotube diameter decreases, more states fall behind the centrifugal barrier, which is consistent with a  $l^2/\rho^2$  scaling of the centrifugal potential. In the case of (12,0) SWNT ( $a=0.47$  nm)  $l_{\text{barrier}}=5$ , and in the case of (9,0) SWNT ( $a=0.35$  nm)  $l_{\text{barrier}}=4$  (see Fig. 4). The movement of the centrifugal barrier toward the nanotube surface caused by the decrease in the nanotube diameter rules out the possibility of scaling the corresponding binding energies. In fact, the major trends in the diameter dependence of the SWNT energy spectrum, evident from Fig. 4, are rather interesting. Energies of low angular momentum states,  $E_{1,l}$  ( $0 \leq l \leq l_{\text{barrier}}$ ), for nanotubes with smaller diameters are located closer to the vacuum level, however, their interlevel separations increase. This is primarily attributed to the different radial dependence of the two components entering Eq. (4) for the effective long-range potential.

In contrast to the decay mechanism of tubular image states, which are shielded from interactions with the surface by means of a centrifugal barrier, the low-angular momentum states can enter the bulk region of a nanotube acquiring finite decay widths owing to their coupling with bulk electronic states. In principle, the quantum-mechanical calculation of image-potential state linewidths,  $\Gamma$ , and the associated lifetimes,  $\tau$ , requires a separate treatment of different nanotube geometries through modeling their bulk electronic structure, and invokes a many body treatment of the decay dynamics, which is beyond the scope of this study. Moreover, results from such an elaborate calculation, can only be used as a qualitative guide, since the experimental disentanglement of contributions from different types of nanotubes is still out of reach.

As a viable alternative, in the present work, the lifetime of an image-potential state  $\psi_{n,l}$  is evaluated by studying the wave function penetration

$$P_{n,l} = \int_0^{a+\Delta R/2} d\rho \psi_{n,l}^*(\rho) \psi_{n,l}(\rho) \quad (8)$$

into the bulk. Previously, this approach was employed for studying lifetimes of image-potential states above surfaces of noble metals. In particular, it was shown that the linewidth of the first image-potential state at the  $\bar{\Gamma}$  point of Cu(111) is proportional to the penetration depth<sup>27</sup> of its wave function. Subsequent measurements utilizing the femtosecond time-resolved photoemission have confirmed that the lifetime of  $n=1$  state strongly depends on the penetration of an image electron into the crystal and is not very sensitive to the detailed form of the wave function.<sup>24</sup> It should be noted, however, that the above conclusion is valid only for image-potential states that are located within an energy gap in the projected band structure along the surface normal and, therefore, decay dominantly through inelastic effects associated with electron-hole pair excitations. For states that are located outside the gap and, thus, degenerate with the continuum of energy in the conduction band, the dominant contribution to the linewidth will be elastic, in which case, their lifetimes cannot be deduced from wave function penetrations.

TABLE I. Calculated penetrations of the  $l=0$ ,  $n=1-5$  image-potential state wave functions into a (10,10) SWNT nanotube. The second row shows the expected ratio of lifetimes,  $\tau_n/\tau_1$ .

| $n$                             | 1     | 2     | 3     | 4     | 5     |
|---------------------------------|-------|-------|-------|-------|-------|
| Penetration (%)                 | 0.592 | 0.264 | 0.151 | 0.055 | 0.038 |
| Lifetime ratio, $\tau_n/\tau_1$ | 1.00  | 2.24  | 3.92  | 10.76 | 15.58 |

The absence of the band structure in the transverse direction of a nanotube favors the assumption that the dominant decay channel in SWNTs is inelastic. Hence, image-potential state lifetimes are predominantly influenced by their wave function penetrations beyond the tube's surface. The penetration depth, Eq. (8), in this case, provides a measure of the coupling of the state  $\psi_{n,l}$  to bulk electronic states. This coupling, weighted by the screened interaction, is responsible for the decay of image-potential states through electron-hole pair excitations. Within this heuristic approximation, the linewidth of a state can be related to its penetration depth by

$$\Gamma(E_{n,l}) \propto P_{n,l} \Gamma_{\text{bulk}}(E_{n,l}), \quad (9)$$

where  $\Gamma_{\text{bulk}}(E_{n,l})$  is the linewidth of a bulk state corresponding to the energy  $E_{n,l}$ . For metal surfaces an empirical energy scaling for the quantity  $\Gamma_{\text{bulk}}$  as a linear power of the image state energy with respect to the Fermi energy has been obtained,<sup>28</sup> for the free electron gas this scaling is found to be quadratic.<sup>29</sup> Considering for a nanotube an energy scaling to be some power of  $(E_{n,l}-E_F)$ , we note that the value of  $\Gamma_{\text{bulk}}$  is largely independent of image state energies of the tube since  $E_F$  is much larger than a typical value of  $E_{n,l}$ . Therefore, a good estimate of the ratio of the lifetimes can be obtained from the ratio of the penetration depths.

Table I shows the probabilities for a zero-angular momentum image electron to be inside a (10,10) SWNT ( $\rho \leq a + \Delta R/2$ ). As expected, the increase in the principal quantum number of an image-potential state results in smaller penetrations of its wave function into the nanotube, increasing the lifetime of the state. Noticeably, the typical penetration depth for a nanotube state is found to be less than 1%, which is substantially smaller than the average penetration depths of image-potential states above metal surfaces. The latter can extend up to 35–40% into the crystal [for  $n=1$  of Cu(111)], corresponding to lifetimes of 8–10 fs.<sup>24</sup> It should be emphasized that following the above discussion, the calculated penetration probabilities can be used only for predicting the relative lifetimes of image-potential states within a certain nanotube geometry. Thus, scaling of linewidths according to the difference in the penetration depths between the image-potential states above a Cu(111) surface and a (10,10) SWNT is not likely to yield accurate lifetimes. Qualitatively, however, the comparison of penetration probabilities indicates that electron-pair excitation cross sections for image-potential states in SWNTs are smaller than in surfaces, and, as a result, their lifetimes are expected to be longer.

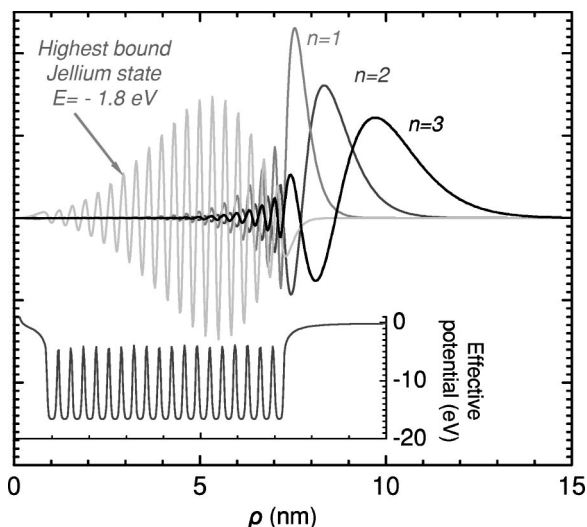


FIG. 5. Wave functions for the lowest three image-potential states calculated for 19-walled ( $d=14.2$  nm) MWNT ( $l=1$ ). Wave function for the highest bound state forming within the jellium shell is also shown. The lower panel displays the total effective potential in radial direction.

**B. Multiwalled nanotubes**

Similar to SWNTs, MWNTs offer numerous potential applications. Their synthesis, on the other hand, is relatively inexpensive and yields large quantities of isolated tubes. Thus, at least for the moment, probing the existence of image-potential states in a MWNT could be more accessible experimentally, especially since the appearance of MWNTs in the sample is more suitable for the formation of these states.

The investigated nanotubes are constructed from 12–19 coaxial single-walled shells, separated from each other by 0.34 nm,<sup>30–32</sup> which is the spacing of a turbostratic graphite. For this arrangement, the diameter of the outer SWNT is 9.48–14.21 nm. The total effective potential, calculated according to the discussion in Sec. II is shown in the inset of Fig. 5. The penetration depth of an image electron beyond the surface plane ( $\rho=a$ ) of a MWNT can be seen in Fig. 5, where the wave functions for the first three image-potential states are shown. For comparison, the wave function for the highest bound electronic state forming inside the nanotube is also displayed. Even in the case of the  $n=1$  cluster of image-potential states, the probability for an electron to be found inside the outermost jellium well is negligible. Thus, at least for image-potential interactions, a MWNT can be effectively replaced with a SWNT located in the outer shell. In this case, arguments concerning the diameter dependent properties of a SWNT spectrum should be also applicable to MWNTs. This claim is clearly supported by the spectrum calculated for a MWNT, which is shown in Fig. 6. In comparison with  $E_{n=1,l}$  binding energies of a SWNT displayed in Fig. 4, the energy levels of a MWNT are located further away from the vacuum level.

According to Fig. 6, binding energies of image states in MWNTs are almost insensitive to electron angular momenta. As was mentioned above, the centrifugal interaction is inde-

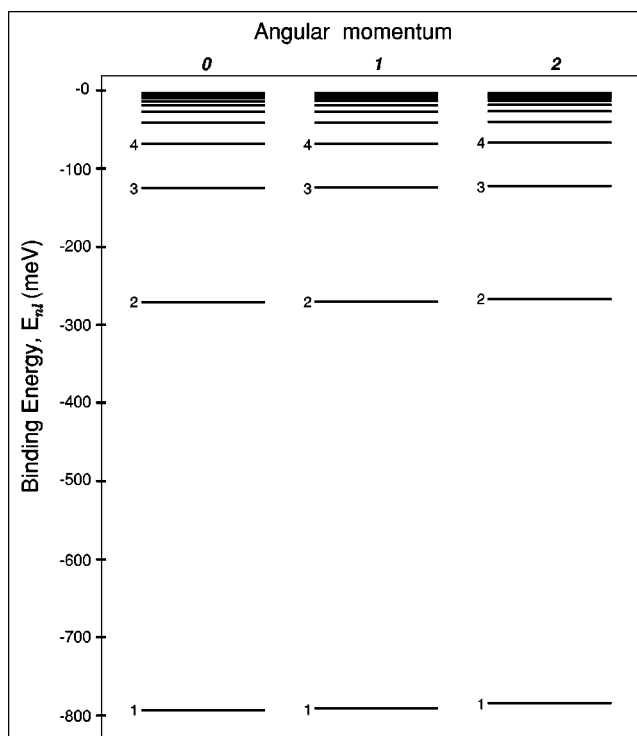


FIG. 6. Binding energies of image-potential states are calculated for the case of a MWNT that has an outer diameter of 9.48 nm. Series of states with angular momenta in the range of 0–2 are considered. Numbers next to the energy bars indicate a state’s principle quantum number,  $n$ .

pendent of the nanotube diameter, whereas the image potential interaction scales as  $\rho/a$ . Clearly, for large diameter nanotubes the angular dependent contribution into the total long-range potential becomes less significant. It is also clear that the minimal value of angular momentum needed for the formation of the positive barrier,  $l_{\text{barrier}}$ , in MWNT will increase. For instance, in the case of the 12-walled MWNT  $l_{\text{barrier}}=14$ . The influence of nanotube parameters on the centrifugal barrier is analyzed in Fig. 7, where the barrier height is plotted versus the electron angular momentum and the nanotube diameter. According to Fig. 7, the formation of this barrier in MWNTs not only requires relatively large values of  $l$  but also has a very slow growth with increasing angular momentum. For instance, the barrier height for the 9.48 nm MWNT is only 0.3 eV, when  $l=25$ . The corresponding binding energies of over-the-barrier image states in MWNTs are estimated to be less than 1 meV away from the vacuum level. Consequently, even a minor fluctuation in the effective potential along the tube, for example due to electron-phonon interaction, will result in the ionization of these states.

**C. Nanotube bundles**

It is well known that SWNTs tend to stick into bundles or ropes during their syntheses.<sup>10</sup> In this case, the effective potential for an electron moving in the vicinity of a nanotube bundle is no longer cylindrically symmetric and, therefore, is inseparable with respect to two coordinates in the plane perpendicular to the axis of a bundle.

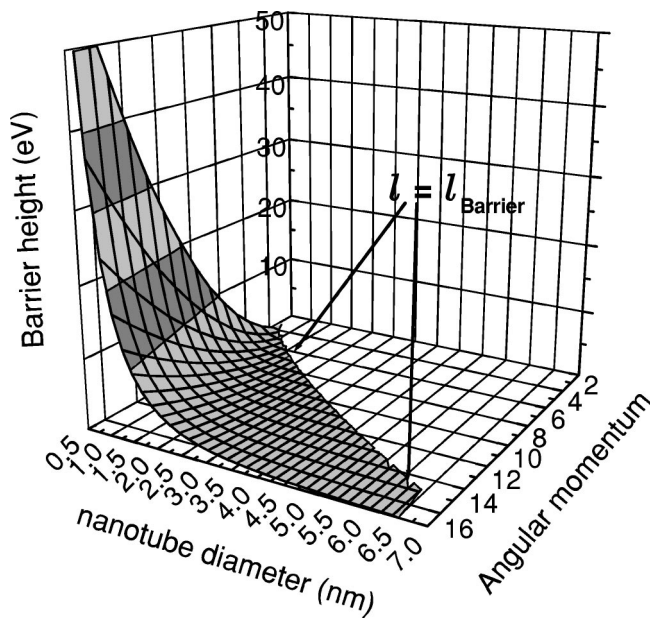


FIG. 7. The height of the positive centrifugal barrier as a function of the electron angular momentum,  $l$ , and the nanotube diameter. The results are valid both for SWNTs and MWNTs (see text). The curve, indicated as  $l=l_{\text{barrier}}$ , is formed by the crossing of the potential surface with the  $XY$  plane, and displays the marginal combination of the nanotube parameters ( $a$  and  $l$ ) needed for the formation of the positive barrier.

In this subsection, an effective long-range potential for nanotube bundle is derived for a simplified case when an electron interacts with only two adjacent SWNTs at a time. This scenario can be realized when nanotube bundles contain just a few SWNTs or when an electron is located close to the surface of the bundle. In this study, the two (12,0) SWNTs are considered in a hexagonal close-packed bundle, which has a characteristic van der Waals separation between adjacent nanotubes,  $\Delta L$ , of approximately 0.3 nm.<sup>33</sup> The potential is calculated for the plane perpendicular to axes of both SWNTs. With these considerations, the effective electron-bundle potential can be approximately given in Cartesian coordinates as a superposition of contributions from individual nanotubes,

$$V(X, Y) = V_{i=0}^{\text{eff}}(\rho_1) + V_{i=0}^{\text{eff}}(\rho_2),$$

$$\rho_i^2 = Y^2 + (X + (-1)^{i-1}(a_i + \Delta L/2))^2 \quad (i = 1, 2), \quad (10)$$

where  $a_i$  are the nanotubes' radii,  $\rho_i$  is the position of an electron in the Cartesian frame of reference, and  $V_{i=0}^{\text{eff}}(\rho)$  is the total effective potential given by Eq. (6) excluding the centrifugal part. In principle, both the interaction of nanotube electrons with core ions of the other nanotube and intertube electron-electron interaction will affect the distribution of the induced image charge. The effective range for both interactions, however, is comparable to the atomic radius of carbon, which is substantially smaller than the diameter of a nanotube. Therefore, in the present analysis, aimed to provide a qualitative illustration of the long-range character of the potential, intertube interactions are neglected.

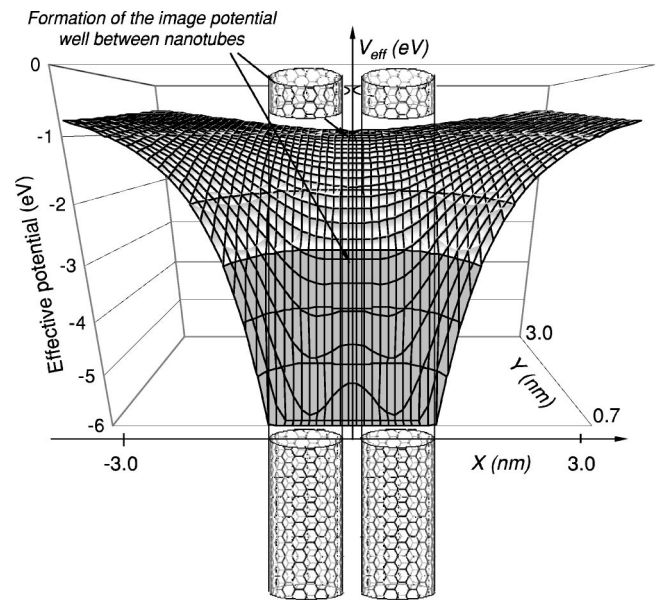


FIG. 8. Effective potential,  $V(x, y)$ , for the two adjacent (12,0) SWNTs. The  $XY$  plane is perpendicular to the axis of both nanotubes.

The resulting potential for the two SWNTs,  $V(X, Y)$ , is shown in Fig. 8, where the  $XY$  Cartesian plane is perpendicular to nanotubes' axes and its origin is located symmetrically between SWNTs.

The form of the potential along the  $X$  axis at 0.0–0.6 nm away from the nanotube's surface ( $Y < 1.1$  nm) has two wells at  $X_{1,2} = \pm(a + \Delta L/2)$ , corresponding to the minima of the jelliumlike potential for each nanotube. The height of the potential barrier, separating these wells in the  $X$  direction decreases as the electron moves away from the nanotubes along the  $Y$  axis. When  $Y \approx 1.1$  individual wells can no longer be distinguished, instead, the projection of  $V(X, Y)$  along the  $X$  axis reveals only one potential well centered at  $X=0$  (between nanotubes). Electronic states supported in this potential can no longer be associated with a single nanotube and should be considered as image-potential states of a bundle. Since the merging of the two individual potential wells into one occurs at distances less than 1.1 nm away from axes of each tube, the full range of image-potential states ( $\psi_{1,0} - \psi_{\infty,0}$ ) associated with an isolated nanotube (see Fig. 2) will be altered by the presence of the second SWNT. The nature of the change in the individual nanotube spectra is defined by the form of the intertube well, which is slightly deeper and approximately twice as wide as the potential well of a single nanotube. Thus, in the present approximation, binding energies of image-potential states in bundles will be more deeply bound than those of isolated SWNTs.

#### IV. CONCLUSIONS

The formation of image-potential states near surfaces of both SWNTs and MWNTs was investigated theoretically. The states are confined between the self-induced potential on the vacuum side and the surface barrier, created by the cen-

tral ascent in the transverse nanotube potential. Binding energies and wave functions were calculated by modeling the interactions inside the nanotube with a cylindrical jelliumlike short-range potential, parameterized to ensure the correct behavior at the bulk–vacuum interface. Calculations were performed for (12,0), (10,10), (9,0) SWNTs and ( $d=9.48$  nm) MWNT utilizing a wide range of electron angular momenta. In addition, the expected relative lifetimes were calculated for the case of zero-angular momentum states of a (10,10) SWNT. Present results indicate a unique dependence of image-potential state properties on the nanotube diameter, which is primarily determined by the different radial behavior of the induced and centrifugal parts in the effective potential for the system. According to the present study, the experimental investigation of image-potential states in nanotubes could be realized by using time-resolved

photoemission.<sup>4</sup> This technique was developed from two-photon photoemission and has proven to be the most versatile in studying unoccupied electronic states on a femtosecond scale. Its typical energy resolution for photoionized electrons is about 10 meV,<sup>26</sup> which would allow for the observation of individual image-potential states. In addition, time-resolved photoemission can map out the temporal evolution of photoexcited electrons, providing an ideal tool for studying the lifetimes of image-potential states in carbon nanotubes.

#### ACKNOWLEDGMENTS

This work was supported by Chemical Sciences, Geosciences and Biosciences Division, Office of Basic Energy Sciences, Office of Science, U. S. Department of Energy.

- 
- <sup>1</sup>D. C. Marinica, C. Ramseyer, A. G. Borisov, D. Teillet-Billy, J. P. Gauyacq, W. Berthold, P. Feulner, and U. Höfer, *Phys. Rev. Lett.* **89**, 046802 (2002).
- <sup>2</sup>D. F. Padowitz, W. R. Merry, R. E. Jordan, and C. B. Harris, *Phys. Rev. Lett.* **69**, 3583 (1992).
- <sup>3</sup>R. W. Schoenlein, J. G. Fujimoto, G. L. Eesley, and T. W. Capehart, *Phys. Rev. Lett.* **61**, 2596 (1988).
- <sup>4</sup>U. Höfer, I. L. Shumay, C. Rruß, U. Thomann, W. Wallauer, and T. Fauster, *Science* **277**, 1480 (1997).
- <sup>5</sup>J. E. Ortega, F. J. Himpsel, R. Haight, and D. R. Peale, *Phys. Rev. B* **49**, 13859 (1994).
- <sup>6</sup>I. G. Hill and A. B. McLean, *Phys. Rev. Lett.* **82**, 2155 (1999).
- <sup>7</sup>P. M. Platzman and M. I. Dykman, *Science* **284**, 1967 (1999); C. C. Grimes and T. R. Brown, *Phys. Rev. Lett.* **32**, 280 (1974).
- <sup>8</sup>P. Glasson, V. Dotsenko, P. Fozooni, M. J. Lea, W. Bailey, G. Papageorgiou, S. E. Andresen, and A. Kristensen, *Phys. Rev. Lett.* **87**, 176802 (2001).
- <sup>9</sup>B. E. Granger, P. Kral, H. R. Sadeghpour, and M. Shapiro, *Phys. Rev. Lett.* **89**, 135506 (2002).
- <sup>10</sup>J. Liu, A. G. Rinzler, H. Dai, J. H. Hafner, R. K. Bradley, P. J. Boul, A. Lu, T. Invernson, K. Shelimov, C. B. Huffman, F. Rodriguez-Marcias, Y. S. Shon, T. R. Lee, D. T. Colbert, and R. E. Smalley, *Science* **280**, 1253 (1998).
- <sup>11</sup>Y. Homma, Y. Kobayashi, T. Yamashita, and T. Ogino, *Appl. Phys. Lett.* **81**, 2261 (2002).
- <sup>12</sup>M. Boyle, K. Hoffmann, C. P. Schulz, I. V. Hertel, R. D. Levine, and E. E. B. Campbell, *Phys. Rev. Lett.* **87**, 273401 (2001).
- <sup>13</sup>M. J. Puska and N. R. Nieminen, *Phys. Rev. A* **47**, 1181 (1993).
- <sup>14</sup>P. J. Jennings, R. O. Jones, and H. Weinert, *Phys. Rev. B* **37**, 6113 (1988).
- <sup>15</sup>N. R. Arista and M. A. Fuentes, *Phys. Rev. B* **63**, 165401 (2001).
- <sup>16</sup>U. Thumm, P. Kürpick, and U. Wille, *Phys. Rev. B* **61**, 3067 (2000).
- <sup>17</sup>E. Zaremba and W. Kohn, *Phys. Rev. B* **13**, 2270 (1976).
- <sup>18</sup>R. O. Jones, P. J. Jennings, and O. Jepsen, *Phys. Rev. B* **29**, 6474 (1984).
- <sup>19</sup>P. Delaney, H. J. Choi, J. Ihm, S. G. Louie, and M. L. Cohen, *Phys. Rev. B* **60**, 7899 (1999).
- <sup>20</sup>Y. K. Kwon, S. Saito, and D. Tománek, *Phys. Rev. B* **58**, R13314 (1998).
- <sup>21</sup>J. W. Mintmire and C. T. White, *Phys. Rev. Lett.* **81**, 2506 (1998).
- <sup>22</sup>S. Reich, C. Thomsen, and P. Ordejón, *Phys. Rev. B* **65**, 155411 (2002).
- <sup>23</sup>K. Horn, K. H. Franck, J. A. Wilder, and B. Reihl, *Phys. Rev. Lett.* **57**, 1064 (1986).
- <sup>24</sup>M. Wolf, E. Knoesel, and T. Hertel, *Phys. Rev. B* **54**, R5295 (1996).
- <sup>25</sup>P. Nikolaev, M. J. Bronikowski, R. K. Bradley, F. Rohmund, D. T. Colbert, K. A. Smith, and R. E. Smalley, *Chem. Phys. Lett.* **313**, 91 (1999).
- <sup>26</sup>T. Hertel, R. Fasel, and G. Moos, *Appl. Phys. A: Mater. Sci. Process.* **75**, 449 (2002).
- <sup>27</sup>P. de Andrés, P. M. Echenique, and F. Flores, *Phys. Rev. B* **35**, 4529 (1987).
- <sup>28</sup>J. B. Pendry, in *Photoemission and the Electronic Properties of Surfaces*, edited by B. Feuerbacher, B. Fitton, and R. F. Willis (Wiley, New York, 1978); D. Li, P. A. Dowben, J. E. Ortega, and F. J. Himpsel, *Phys. Rev. B* **47**, 12895 (1993).
- <sup>29</sup>P. M. Echenique, J. M. Pitarke, E. V. Chulkov, and A. Rubio, *Chem. Phys.* **251**, 1 (2000).
- <sup>30</sup>C. H. Kiang, M. Endo, P. M. Ajayan, G. Dresselhaus, and M. S. Dresselhaus, *Phys. Rev. Lett.* **81**, 1869 (1998).
- <sup>31</sup>A. N. Kolmogorov and V. H. Crespi, *Phys. Rev. Lett.* **85**, 4727 (2000).
- <sup>32</sup>M. F. Yu, O. Lourie, M. J. Dyer, K. Moloni, T. F. Kelly, and R. S. Rouf, *Science* **287**, 637 (2000).
- <sup>33</sup>J. Tang, L.-C. Qin, T. Sasaki, M. Yudasaka, A. Matsushita, and S. Iijima, *Phys. Rev. Lett.* **85**, 1887 (2000).